PCCP

ROYAL SOCIETY OF CHEMISTRY

PAPER

View Article Online
View Journal | View Issue

Cite this: *Phys. Chem. Chem. Phys.*, 2024, **26**, 5858

The heterointerface effect to boost the catalytic performance of single atom catalysts for sulfur conversion in lithium–sulfur batteries†

Haikuan Liang, Zhihao Zeng, Zhengping Qiao,* Yan Li* and Chengxin Wang

Lithium–sulfur (Li–S) batteries are considered as one of the promising next-generation energy storage devices due to their characteristics of high energy density and low cost. However, the shuttle effect and sluggish conversion of lithium polysulfide (LiPs) have hindered their commercial applications. To address these issues, in our previous works, we have screened several highly efficient single atom catalysts (SACs) (MN_4@G, M = V, Mo and W) with atomically dispersed transition metal atoms supported by nitrogen doped graphene based on high throughput calculations. Nevertheless, they still suffer from low loading of metal centers and unsatisfactory capability for accelerating the reaction kinetics. To tackle such problems, based on first-principles calculations, we systematically investigated the heterointerface effect on the catalytic performance of such three MN_4@G toward sulfur conversion upon forming heterostructures with 5 typical two-dimensional materials of TiS_2, C_3N_4, BN, graphene and reduced graphene oxide. Guided by efficient descriptors proposed in our previous work, we screened VN_4@G/TiS_2, MoN_4@G/TiS_2 and WN_4@G/TiS_2 possessing low Li_2S decomposition barriers of 0.54, 0.44 and 0.41 eV, respectively. They also possess enhanced capabilities for catalyzing the sulfur reduction reaction as well as stabilizing soluble LiPs. More interestingly, the heterointerface can enhance the capability of the carbon atoms far away from the metal centers for trapping LiPs. This work shows that introducing a heterointerface is a promising strategy to boost the performance of SACs in Li–S batteries.

Received 3rd December 2023,
Accepted 19th January 2024

DOI: 10.1039/d3cp05883b

rsc.li/pccp

1. Introduction

To reduce the greenhouse gas emission caused by the consumption of fossil fuels stimulates great interest from researchers to develop high-performance energy storage devices. Among these state-of-the-art energy storage devices, lithium–sulfur (Li–S) batteries have garnered significant attention in recent years owing to their high theoretical specific capacity of 1675 mA h g^{-1} and high energy density of 2600 W h kg^{-1}.[1–5] However, certain issues still exist, weakening the performance of Li–S batteries and thus impeding their commercial applications. The most significant issue among them is the occurrence of the 'shuttle effect'. During the discharge process, lithium polysulfides (LiPs) formed on the cathode can dissolve into the electrolyte, diffuse through the separator, and accumulate on the lithium anode. This phenomenon leads to a decrease in the Coulombic efficiency and capacity degradation of the batteries, thus hindering their cycle performance.[6,7] Moreover, the intrinsic insulation properties of sulfur (5×10^{-30} S cm^{-1}) and Li_2S (10^{-13} S cm^{-1}) hinder the efficient transfer of electrons, resulting in sluggish electrochemical reactions.[8] Therefore, the rational design of catalysts exhibiting suitable adsorption capability for LiPs and superior catalytic performance for accelerating the reaction kinetics of sulfur redox in Li–S batteries has attracted increasing research attention in recent years.[9–12]

Among the efficient catalysts, carbonaceous materials supported single atom catalysts (SACs) have been widely explored due to their superior catalytic performance for sulfur redox and LiP stabilization.[10,13–15] Nevertheless, the performances of SACs for catalyzing sulfur redox, particularly the sulfur evolution reaction (SER), are still unsatisfactory. Therefore, to further enhance their catalytic performance toward the sulfur conversion is of importance, which might be realized by tailoring the electronic and structural properties of the central metals of SACs. In this regard, significant research efforts have been devoted to the design of SACs with transition metal atoms possessing various coordination environments, which involve

State key Laboratory of Optoelectronic Materials and Technologies, School of Materials Science and Engineering, Sun Yat-sen (Zhongshan) University, Guangzhou 510275, People's Republic of China. E-mail: cesqzp@mail.sysu.edu.cn, liyan266@mail.sysu.edu.cn

† Electronic supplementary information (ESI) available: Computational details; structure information of heterostructure materials; additional figures and tables. See DOI: https://doi.org/10.1039/d3cp05883b

graphene,[13,14] C_2N[10] and g-C_3N_4[15] as the supports. In addition to doping strategies, the introduction of heterointerfaces has also been proved to be an efficient strategy to enhance the catalytic performance of electrochemical catalysts for energy storage and conversion, which can be realized by assembling two-dimensional (2D) materials into van der Waals heterostructures.[16] These heterostructures are formed by chemical bonding or physical combination of two or more 2D materials. In recent years, this concept has also been adopted to design electrocatalysts for Li–S batteries, which will incorporate the merits of individual components to neutralize the shortcomings of each building block[17–22] of the heterointerfaces. Nevertheless, there have been no reports on exploring the heterointerface effect on the catalytic performance of SACs for sulfur chemistry.

Up to now, various materials have been investigated for use as electrodes including 2D carbonaceous materials,[23,24] metal sulfides,[25,26] metal oxides[27,28] and Mxenes.[29,30] This implies that the combination of SACs with such materials will give rise to a huge number of heterostructures given the various metal centers of SACs. In this regard, to explore the catalytic performance particularly the SER performance of such heterostructures will be very time consuming, which accordingly requires an efficient descriptor guiding the systematic investigation. In our previous work, we have systematically investigated the descriptors of the Li_2S decomposition energy barrier on MN_4@G (typical configuration of SACs containing pyridine-N coordinated transition-metal atoms) and found that some properties could serve as universal descriptors for the rational design of SACs giving rise to a low Li_2S decomposition barrier, which could predict the activity of the catalyst quickly.[14]

Here, we investigated systematically the performance of heterostructures for sulfur chemistry, which are built by combining SACs with 5 typical 2D materials. For SACs, we utilized three MN_4@G (M = V, Mo and W) with the highest catalytic activity for Li_2S decomposition screened in our previous work.[14] The other 5 types of 2D materials are TiS_2,[31] C_3N_4,[32] BN,[33] graphene (G)[34] and reduced graphene oxide (rGO).[35] After examining the extendibility, we selected ΔE (energy difference before and after the Li_2S decomposition) as the efficient descriptor for screening several heterostructures with enhanced catalytic performance for Li_2S decomposition, which were then further explored for their performance for catalyzing SRR and stabilizing LiPs. Our work will pave a new way for designing electrocatalysts for sulfur chemistry in alkaline metal sulfide batteries.

2. Computational details

The DFT simulations were carried out by using the Vienna Ab initio Simulation Package (VASP).[36,37] Additionally, the Perdew–Burke–Ernzerhof functional[38,39] within the generalized gradient approximation (GGA-PBE)[40] was employed to calculate the exchange–correlation energy and the projector augmented wave (PAW) method was used to describe the electron–ion interactions.[41,42] We employed the DFT-D2 scheme to take the van der Waals interactions into account.[43] To avoid the interaction between two neighboring surfaces, we set the vacuum space to be larger than 20 Å. In all of the calculations, the plane-wave cutoff energy was set to be 520 eV. All the calculations were carried out with the force and energy thresholds of 0.02 eV $Å^{-1}$ and 10^{-4} eV, respectively. Self-consistent field (SCF) calculations were performed to obtain the energy of the optimized structure while non-self-consistent field (NSCF) calculations were used to gain the electronic density of states (DOS). Three different k-point meshes of $2 \times 2 \times 1$, $3 \times 3 \times 1$ and $7 \times 7 \times 1$ were employed in the structural optimizations, and SCF and NSCF calculations. For the Li_2S decomposition, the minimum energy path (MEP) profiles are obtained by using the climbing image nudged elastic band (CI-NEB) method.[44,45] The formulas for calculating binding energy of heterostructure materials, lattice mismatch of the heterostructure materials, adsorption energy, zero vibration energy, charge density difference and Gibbs free energy changes are labeled as eqn (1)–(10).

The binding energy of heterostructures were calculated according to

$$E_{\text{bin}} = \frac{E_{\text{total}} - E_{\text{ML1}} - E_{\text{ML2}}}{S} \quad (1)$$

where E_{total} represent the energies for heterostructures, E_{ML1} and E_{ML2} stand for the energy of two individual monolayers constituting the heterostructures, respectively, S is the cross-sectional area at the interface of two monolayers in the simulation box of the heterostructures. Additionally, the lattice mismatch of the heterostructures is calculated by

$$|a - a_{\text{h}}|/a_{\text{h}} \times 100\% \quad (2)$$

where a and a_{h} represent the lattice parameter of the supercell of one component and the double layer heterostructure material, respectively.

The adsorption energy (E_{ads}) is calculated based on the following formula:

$$E_{\text{ads}} = E_{\text{total}} - E_{\text{substrate}} - E_{\text{adsorbate}} \quad (3)$$

where E_{total} is the energy of adsorbed system, while $E_{\text{substrate}}$ and $E_{\text{adsorbate}}$ represent the energy of substrate and isolated adsorbate, respectively.

The Gibbs free energy of LiPs and S_8 on substrates are calculated by

$$G = E_{\text{DFT}} + E_{\text{zpe}} - TS \quad (4)$$

where E_{DFT} denotes the energy calculated by DFT simulations and E_{zpe} is the zero-point energy which is determined as $\text{ZPE} = \frac{1}{2}\sum_i h\nu_i$; here h and ν_i are the Planck constant and vibrational frequencies, respectively. S is the entropy, the entropies of molecules we utilized were acquired from experimental values in the NIST database,[46] while those of the absorbed intermediates were set to zero; T is the room temperature and is set at 298.15 K.

The elementary reaction steps for sulfur reduction in lithium–sulfur (Li–S) batteries are considered as

$$S_8 + 16Li^+ \rightarrow S_8^* + 16Li^+ \quad (5)$$

$$S_8^* + 16Li^+ + 2e^- \rightarrow Li_2S_8^* + 14Li^+ \quad (6)$$

$$Li_2S_8^* + 14Li^+ + 2e^- \rightarrow Li_2S_6^* + Li_2S_2 + 12Li^+ \quad (7)$$

$$Li_2S_6^* + Li_2S_2 + 12Li^+ + 2e^- \rightarrow Li_2S_4^* + 2Li_2S_2 + 10Li^+ \quad (8)$$

$$Li_2S_4^* + 2Li_2S_2 + 10Li^+ + 2e^- \rightarrow Li_2S_2^* + 3Li_2S_2 + 8Li^+ \quad (9)$$

$$Li_2S_2^* + 3Li_2S_2 + 8Li^+ + 8e^- \rightarrow Li_2S^* + 7Li_2S \quad (10)$$

The reduction reaction process from Li_2S_8 to Li_2S is quite complex, which is accompanied with the formation of the by-product Li_2S_2.[47] The energy of a single Li ion and an electron ($Li^+ + e^-$) pair was treated as the energy of a single crystalline Li atom. The absorbents with an asterisk "*" refer to the state of being adsorbed, while the isolated state does not have that mark.

The linear correlations between E_b and three descriptors ΔE, ΔE(*LiS) and ICOHP were identified in our previous work.[14]

$$E_b = 1.07 \times \Delta E + 0.16 \quad (11)$$

$$E_b = 0.87 \times \Delta E(*LiS) + 0.38 \quad (12)$$

$$E_b = -1.30 \times ICOHP - 3.49 \quad (13)$$

The difference between ΔE and ΔE(*LiS) is shown below,

$$\Delta E = E(*Li + *LiS) - E(*Li_2S) \quad (14)$$

where E(*Li + *LiS) and E(*Li_2S) represent the energies of final and initial states of the Li_2S decomposition. The asterisk (*) means the adsorbed state of the adsorbents.

$$\Delta E(*LiS) = E(*LiS) + E(Li)_{bcc} - E(*Li_2S) \quad (15)$$

where E(*LiS), $E(Li)_{bcc}$, E(*Li_2S) refer to the total energy of the adsorbed LiS cluster, energy of single Li atom in the bcc bulk phase and total energy of adsorbed Li_2S, respectively.

3. Results and discussion

3.1 Structure and electronic properties of heterostructures

As shown in Fig. 1, five types of monolayers, which are TiS_2, g-C_3N_4, BN, graphene, and rGO, are selected and combined with MN_4@G to build heterostructures. Due to the different lattice parameters of those monolayers, various supercells are set up for TiS_2, g-C_3N_4, BN, graphene and rGO to guarantee a small lattice mismatch in the heterostructure. The primitive cell parameters, corresponding supercells, lattice mismatches and the total number of atoms contained in the simulation box of the heterostructures are listed in Table S1 (ESI†). Regarding the model of rGO and MN_4@G, they are built using a 6 × 6 × 1 supercell of graphene. rGO is then achieved by introducing two kinds of oxygen-containing defects in the graphene lattice. One type refers to the vacancy defects with hydroxyl saturating the dangling bonds of carbon atoms and the other type includes the epoxide functional groups adsorbed on the carbon atoms while the MN_4@G are modeled by locating the TM atoms in the N doped graphene with the central metal atoms coordinated with four N atoms, which are accordingly labeled as MN_4@G. The largest lattice mismatch is 2.354% between TiS_2 and MN_4@G, and the others are lower than 2% when MN_4@G

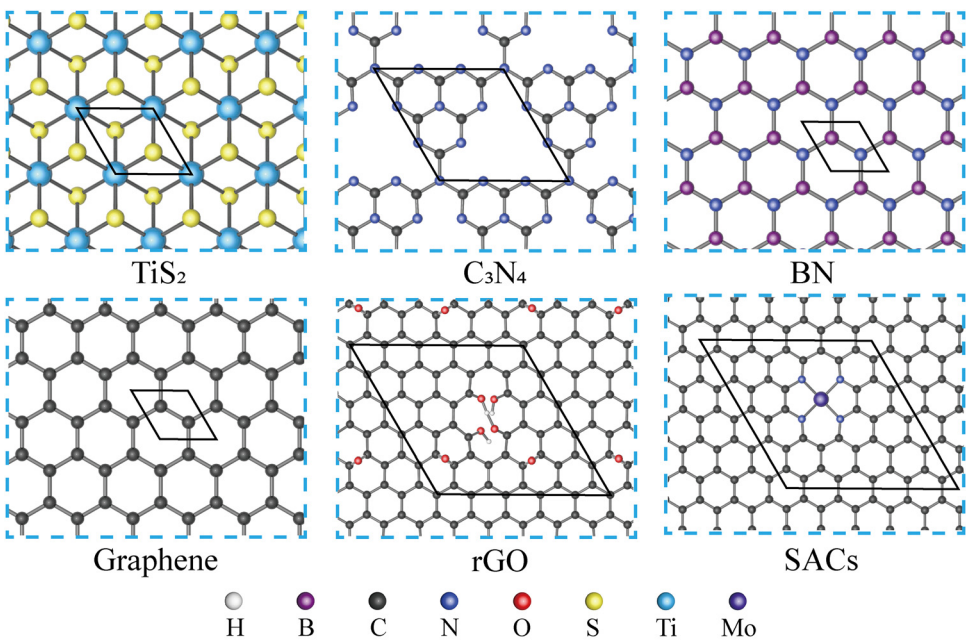

Fig. 1 Top view of TiS_2, C_3N_4, BN, graphene, rGO and SACs. The hexagonal line frames depict the primitive cells of various materials, while the elements represented by spheres of different colors are listed at the bottom of the figure. For SACs, MoN4@G is selected as an example.

forms heterostructures with g-C_3N_4(1.777%), BN(1.749%), graphene(0.000%) and rGO(1.211%). In order to distinguish those various heterostructures, we named them MN_4@G/ML (ML = TiS_2, C_3N_4, BN, G, rGO), as shown in Fig. S1 (ESI†). Moreover, MN_4@G/ML (ML = TiS_2, C_3N_4, G and rGO) and G/BN prefer AB stacking, while the configuration of MN_4@G/BN possesses a mixture of AB- and AA-stacking.

The interaction strength between the components of the heterostructures can be evaluated by the binding energy (E_{bin}), which is calculated by eqn (1) in the ESI.† As listed in Table S2 (ESI†), the E_{bin} values for different heterostructures are between −13 and −21 meV Å^{-2} and close to that for van der Waals interaction,[48] which can also be confirmed by the interlayer distance of 3.20–3.96 Å. Among them, the largest and smallest E_{bin} are −26.39 meV Å^{-2} (WN_4@G/BN) and −7.49 meV Å^{-2} (MoN_4@G/C_3N_4), respectively. Moreover, MN_4@G can bind more strongly with BN than with other monolayers, while the binding strength of MN_4@G with TiS_2 and C_3N_4 are relatively weak. Among MN_4@G/TiS_2 or MN_4@G/BN, the interaction strength of monolayers as M = V is stronger than that when M = Mo and W, due to the fact that V atom tends to sit between the two monolayers by forming chemical bond with two components of the heterostructures, as shown in Fig. S1 (ESI†). Note that heterostructures of MN_4@G/rGO have significantly larger interlayer distances than the others due to the presence of functional groups on the surface of rGO.

The formation of heterostructures also induces the charge redistribution in the components, *i.e.* MN_4@G loses charges to the adjacent layers leading to the metal centers more positively charged compared to that in the monolayer of MN_4@G. The diagram of charge density difference of various heterostructures are illustrated in Fig. S1 (ESI†). In general, the charge transfer occurs mainly around the MN_4 moiety and the specific values of charge transfer are listed in Table S2 (ESI†). However, for MN_4@G/TiS_2, there is a uniform charge redistribution throughout the interface. In general, the charge transfer between the monolayers in MN_4@G/TiS_2 and MN_4@G/C_3N_4 is more pronounced than that in MN_4@G/BN and MN_4@G/G as illustrated in Table S2 (ESI†). Moreover, for MN_4@G/TiS_2 and MN_4@G/C_3N_4, M = V gives rise to more charge transfer than M = Mo and W. Taking MN_4@G/TiS_2 as an example, the charge transfer in MN_4@G/TiS_2 is 1.48 e per cell, which is more than those in MoN_4@G/TiS_2 (1.11 e per cell) and WN_4@G/TiS_2 (1.11 e per cell). Although the total amount of charge transfer for MN_4@G/BN is less than that for MN_4@G/TiS_2, the interaction between the monolayers is still stronger in MN_4@G/BN than that in MN_4@G/TiS_2. This is attributed to the fact that the charge redistribution only occurs around the MN_4 in the former case while there is wider range of charge redistribution for the rest case.

3.2 Catalytic performance of MN_4@G/ML for SER

We next explored the catalytic performance of the heterostructures for SER. In the charging cycles of Li–S batteries, the decomposition of Li_2S is a crucial step for SER requiring efficient electrocatalysts to accelerate the reaction kinetics. This

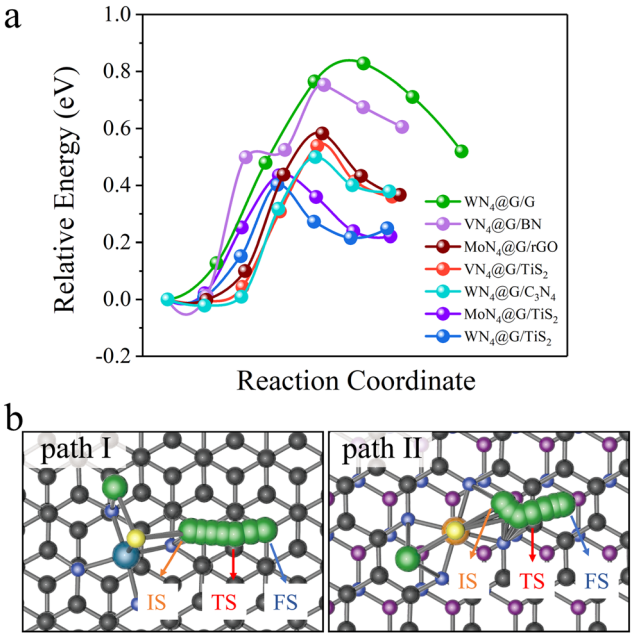

Fig. 2 (a) The energy profiles of Li_2S decomposition on selected heterostructures. (b) Two different energetically preferable Li_2S decomposition pathways. IS, TS, FS represent the initial, transitional, and final states of Li_2S decomposition on the heterointerfaces, respectively.

is usually evaluated by the energy barrier (E_b) of Li_2S decomposition, which can be achieved based on the nudged elastic band (NEB) method.[14]

We selected some heterostructures as representatives and explored the decomposition of Li_2S on them. The energy profiles of Li_2S decomposition on WN_4@G/G, VN_4@G/BN, MoN_4@G/rGO, WN_4@G/C_3N_4, MoN_4@G/TiS_2 and WN_4@G/TiS_2 with the energetically preferable decomposition pathways are illustrated in Fig. 2. It can be seen from Fig. 2a that the E_b of Li_2S decompositions on all heterostructures are lower than 1.0 eV. The lowest and the highest E_b are observed on WN_4@G/TiS_2 (0.41 eV) and WN_4@G/G (0.83 eV), respectively. The catalytic performances of the heterostructures for the Li_2S decomposition follow the order WN_4@G/TiS_2 > MoN_4@G/TiS_2 > WN_4@G/C_3N_4 > VN_4@G/TiS_2 > MoN_4@G/rGO > VN_4@G/BN > WN_4@G/G, and the corresponding E_b values are 0.41, 0.44, 0.50, 0.54, 0.58, 0.75 and 0.83 eV respectively. It should be noted that those heterostructures possess more enhanced capability for catalyzing SER than individual MN_4@G, such as VN_4@G (E_b = 0.70 eV), MoN_4@G (E_b = 0.58 eV), WN_4@G (E_b = 0.55 eV) and CoN_4@G (E_b = 1.37 eV).[13,14] Overall, the catalytic performance of MN_4@G for the SER will be significantly improved when forming the heterostructures with C_3N_4, TiS_2 and rGO. Moreover, due to the different adsorption configurations of Li_2S, two different Li_2S decomposition pathways are identified as shown in Fig. 2b. And the cleavage of the Li–S bond on WN_4@G/G is along the path I, while for the rest cases it follows the relatively short path II.

It should be noted that the decomposition of Li_2S on VN_4@G/TiS_2 is a bit complex as reflected by the energy profiles of Li_2S decomposition (see Fig. 3a). This is due to the specific

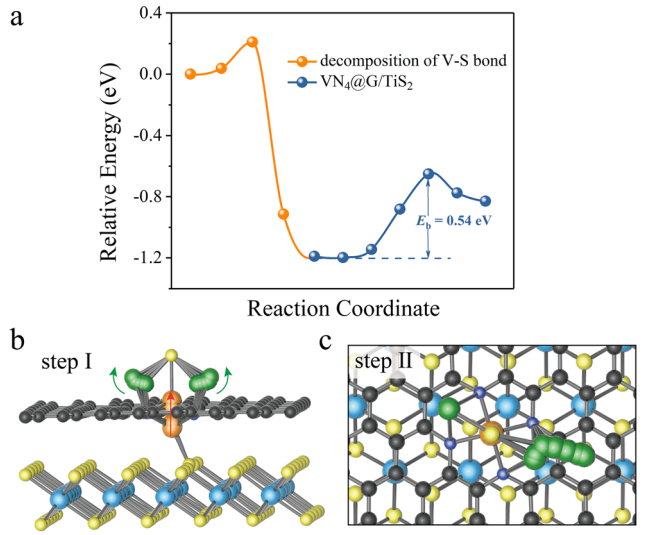

Fig. 3 (a) The energy profiles of Li_2S decomposition on VN_4@G/TiS_2. (b) The structural evolution before the Li_2S decomposition on VN_4@G/TiS_2. (c) The decomposition process of Li_2S on VN_4@G/TiS_2. The migration of V atom follows the direction of the red arrow while the change of angle of Li–S–Li is marked with green arrows.

structural configuration of VN_4@G/TiS_2, for which the V atom sits between the graphene layer and TiS_2 (see Fig. 3b). This further leads to the weak interaction between Li_2S and the V atom upon the adsorption of Li_2S on VN_4@G/TiS_2 since the S atom of Li_2S cannot form a chemical bond with the V atom with only the Li atoms binding to N/C atoms from the N doped graphene. Overall, the whole process of Li_2S decomposition on VN_4@G/TiS_2 can be divided into two subprocesses. Firstly, before the breakage of Li–S bonds in adsorbed Li_2S, the V atom moves back to the center of the N edged hole and binds to the S atom of adsorbed Li_2S, leaving the V–S (S from TiS_2) bond broken (see Fig. 3b). This process just requires overcoming a very small energy barrier of 0.21 eV as shown in Fig. 3a. Meanwhile, the angle of Li–S–Li bond gradually increases from 85.01° to 139.29° and the bond length of Li–S also expands from 2.25 Å to 2.39 Å. It is then followed by the second subprocess of Li_2S decomposition accompanied by the Li–S bond breakage as shown in Fig. 3c (consistent with the decomposition pathway II in Fig. 2b), which necessitates surmounting an energy barrier of 0.54 eV.

It is time-consuming to calculate directly the E_b values for 15 heterostructures using the CI-NEB method. In our previous works, we have identified three descriptors ΔE, ΔE(*LiS) and ICOHP correlating well with E_b for MN_4@G, where ΔE refers to the energy difference between the initial and final states of the Li_2S decomposition, ΔE(*LiS) stands for the reaction energy of the Li_2S decomposition and ICOHP means the integral value of the crystal orbital Hamilton population for evaluating the binding strength of Li–S in adsorbed Li_2S.[14] And the corresponding functions describing the linear correlations between E_b and ΔE, ΔE(*LiS), ICOHP are shown in the computational details. Among them, ΔE performs the best in predicting E_b values. Based on the available data from the current study, we next explored the predictive capability of ΔE, ΔE(*LiS), ICOHP for determining E_b and then to screen high performance MN_4@G/ML for Li_2S decomposition. As shown in Fig. 4a, all the data points of E_b fall near the line, implying the robustness of the functional of $E_b = 1.07 \times \Delta E + 0.16$ proposed in our previous work.[14] The minimum percentage error of E_b between the ΔE–E_b prediction and the CI-NEB calculation occurs in VN_4@G/TiS_2, which is only 2.22%. The largest percentage error is observed in WN_4@G/C_3N_4, reaching 14%, but the specific difference is only 0.07 eV. The percentage errors of the predicted values with respect to those obtained from CI-NEB calculations for the remaining structures are all below 10%. In contrast, the ΔE(*LiS)–E_b and ICOHP–E_b relationships from the current study do not follow the trend described by those linear functions obtained from previous works (see Fig. 4b and c). The corresponding data of predicted E_b values based on ΔE, ΔE(*LiS) and ICOHP are listed in Table S3 (ESI†). Overall, these results show that ΔE can serve as the best descriptor and provide efficient theoretical guidance for fast screening of active MN_4@G/ML toward Li_2S decomposition based on the equation of $E_b = 1.07 \times \Delta E + 0.16$.

As listed Table S3 (ESI†), the E_b values are predicted based on the linear function $E_b = 1.07 \times \Delta E + 0.16$ for 15 heterostructures which are built by combining 3 MN_4@G with 5 monolayers. Among them, MoN_4@G/TiS_2 and WN_4@G/TiS_2 give rise to significantly low E_b values of 0.40 and 0.43 eV,

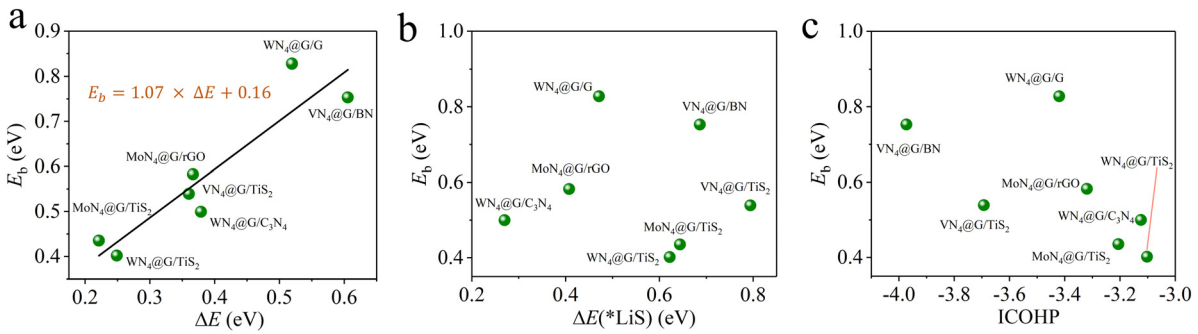

Fig. 4 Calculated values of E_b using the CI-NEB method (green balls) for representative heterostructures as a function of ΔE (a), ΔE(*LiS) (b) and ICOHP (c). In (a), the linear relationship (black lines), obtained in our previous works for graphene supported SACs was included for comparison.[14]

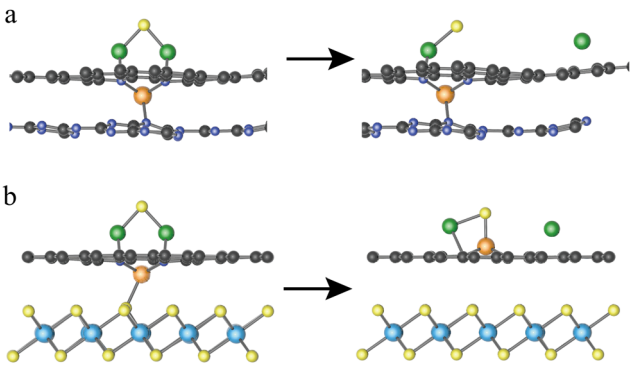

Fig. 5 Initial and final structures of Li_2S decomposition on VN_4G/C_3N_4 (a) and $VN_4@G/TiS_2$ (b). The orange, yellow, green spheres represent the V, S and Li atoms.

Table 1 Comparison of E_b (eV) between heterostructures and their corresponding $MN_4@G$

	Heterostructures	$MN_4@G$
$WN_4@G/TiS_2$	0.41[a]	0.55
$MoN_4@G/TiS_2$	0.44[a]	0.58
$VN_4@G/TiS_2$	0.54[a]	0.70
$WN_4@G/C_3N_4$	0.50[a]	0.55
$MoN_4@G/C_3N_4$	0.57[b]	0.58
$VN_4@G/C_3N_4$	2.24[b]	0.70
$WN_4@G/BN$	0.62[b]	0.55
$MoN_4@G/BN$	0.63[b]	0.58
$VN_4@G/BN$	0.75[a]	0.70
$WN_4@G/rGO$	0.54[b]	0.55
$MoN_4@G/rGO$	0.58[a]	0.58
$VN_4@G/rGO$	0.79[b]	0.70
$MoN_4@G/G$	0.74[b]	0.55
$WN_4@G/G$	0.83[a]	0.58
$VN_4@G/G$	0.79[b]	0.70

[a] E_b values obtained based on the NEB method. [b] E_b values predicted by the E_b–ΔE relationship.

which are accordingly highly efficient for catalyzing the SER. In contrast, the worst SER performance is found for $VN_4@G/C_3N_4$ with E_b = 2.24 eV since the V center does not participate in activating the Li–S bond. As shown in Fig. 5a, in $VN_4@G/C_3N_4$ the V atom tends to sit between the graphene and C_3N_4 monolayers leading to the absence of S–V bonds upon the Li_2S deposition indicating that there is no direct interaction between Li_2S and the V center. Moreover, this holds for the whole process of Li_2S decomposition. Therefore, the catalytic performance of $VN_4@G/C_3N_4$ for Li_2S decomposition is rather worse compared to the rest of the heterostructures. It should be noted that, in the $VN_4@G/TiS_2$ the V atom remains between graphene and TiS_2 monolayers after the Li_2S adsorption. However, during the Li_2S decomposition the V atom can move back the N-edged hole and form a chemical bond with S from Li_2S by overcoming a low energy barrier of 0.21 eV (see Fig. 2a). This S–V bond even remains when the Li–S bond is eventually broken as shown in Fig. 5b. Therefore, $VN_4@G/TiS_2$ still shows efficient SER performance by giving rise to a low E_b of 0.54 eV.

We next analyzed the heterointerface effect on the catalytic performance of $MN_4@G$ for SER. To this end, three SACs of $WN_4@G$, $MoN_4@G$, and $VN_4@G$, screened by our previous work[14] were considered to explore the changes of E_b before and after forming the heterointerfaces. Table 1 shows a comparison of E_b values between $MN_4@G$ and $MN_4@G/ML$ (M = V, Mo and W; ML = TiS_2, C_3N_4, BN, G and rGO). The energy barriers of Li_2S decomposition over $MN_4@G$ are decreased when forming the heterostructures with TiS_2, C_3N_4 and rGO. Among them, TiS_2 provides the best effect on surface regulation leading to enhanced SER performance of $MN_4@G$ by giving rise to E_b of 0.41, 0.44 and 0.54 for $WN_4@G/ML$, $MoN_4@G/TiS_2$ and $VN_4@G/TiS_2$, respectively, while the effect of C_3N_4 and rGO on enhancing the catalytic activity for SER was significantly weak. In contrast, BN and G actually increased the E_b on $VN_4@G$ and $WN_4@G$, respectively, indicating decreased SER performances. Note that the $VN_4@G/C_3N_4$ gives rise to the E_b value of 2.24 eV significantly larger than that of 0.70 eV given by $VN_4@G$. This is due to the fact that the V atom does not participate in catalyzing the Li_2S decomposition. As shown in Fig. 5a, during the whole process of Li_2S decomposition, no chemical bond is formed between the Li_2S cluster and the atomically dispersed V atom sitting between $VN_4@G$ and C_3N_4.

3.3 Heterointerface effect on the performance of $MN_4@G$ for catalyzing SRR and stabilizing LiPs

Since the catalytic performance of SCAs for catalyzing Li_2S decomposition will be significantly enhanced when being combined with TiS_2, we next chose the heterostructures of $MN_4@G/TiS_2$ to further investigate their binding strengths to LiPs and S_8 as well as their SRR performance, which are also crucial for suppressing the shuttle effect as well. In this regard, both sides of the heterostructures were explored. To indicate the specific surface where the adsorbates locate, it is necessary to redefine the nomenclature for the heterostructures. The bilayer consisting of monolayers of ML1 and ML2 can be named ML1/ML2 or ML2/ML1, representing the adsorbate being adsorbed on the side of the ML1 or ML2. For example, $MoN_4@G/TiS_2$ means that MoN_4 provides the active sites for adsorbing the LiPs and S_8 while it means the opposite when it is represented by $TiS_2/MoN_4@G$.

As shown in Fig. 6a and Table S4 (ESI†), the adsorption energies of LiPs on $MN_4@G/TiS_2$ (M = Mo and W) are both below −3.00 eV, which are lower than those on the organic electrolyte molecules such as 1,3-dioxynaphthenes (DOL) and 1,2-dimethoxy ethane (DME) within the range of −1.00 to −0.80 eV.[49] This implies the advantages of such heterointerfaces in suppressing the shuttle effect because the host material exhibits stronger adsorption performance than the organic electrolyte molecules. Moreover, $WN_4@G/TiS_2$ possesses more enhanced capability in trapping LiPs than $MoN_4@G/TiS_2$. In detail, the adsorption energies of LiPs (Li_2S_x, x = 1, 2, 4, 6, 8) and S_8 on the $WN_4@G/TiS_2$ interface are −5.21, −5.15, −4.17, −4.17, −4.33 and −2.52 eV, respectively. They are lower than the corresponding values on $MoN_4@G/TiS_2$, which are −4.67, −3.72, −3.71, −3.35, −3.28 and −2.11 eV, respectively. Note that the adsorption energies on individual TiS_2 and MN4@G are higher than those on the heterostructures as shown in

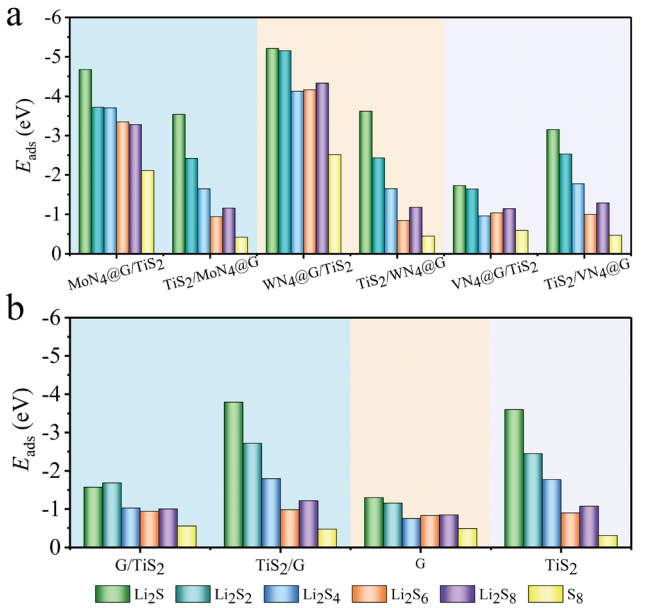

Fig. 6 The bar chart of adsorption energies of LiPs and S_8 on MN_4@G/TiS_2 (a), G/TiS_2, graphene (G) and TiS_2 (b). ML1/ML2 indicates the adsorption site is on ML1.

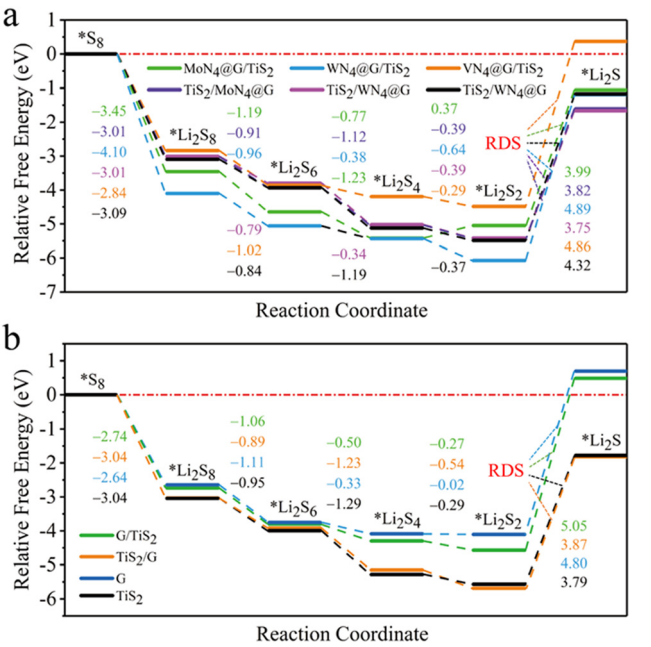

Fig. 7 Gibbs free energy profiles for SRR on MN_4@G/TiS_2 (a), G/TiS_2, graphene (G) and TiS_2 (b). Regarding heterostructures (ML1/ML2), ML1 represents the surface for adsorbing the adsorbates. The numbers with different colors are the Gibbs energy differences between the two adjacent states during SRR.

Table S4. Therefore, the capabilities of MoN_4@G and WN_4@G in stabilizing LiPs are generally enhanced when combined with TiS_2. In contrast, the adsorption strength of VN_4@G/TiS_2 to LiPs and S8 are weaker than that for MN_4@G/TiS_2 (M = Mo and W). The lowest adsorption energy observed on VN_4@G/TiS_2 is merely −1.73 eV for Li_2S adsorption, which means that the adsorption strength of VN_4@G to LiPs is significantly weakened upon forming a heterointerface with TiS_2. This can be attributed to the formation of V–S bonds in the interlamination of VN_4@G/TiS_2. When the reaction intermediates are adsorbed on VN_4@G/TiS_2, the lack of V atoms on the surface of VN_4@G/TiS_2 leads to the absence of chemical bond between V atoms and LiPs/S_8, indicating a relatively weak interaction strength between the heterostructure and LiPs/S_8.

We also considered the binding strength of TiS_2 of three heterostructures to the adsorbates and found that the adsorption energies of various clusters on TiS_2/MN_4@G (M = V, Mo and W) are very similar. Furthermore, the values are comparable to the adsorption on pure TiS_2, suggesting that MN_4@G has a tiny impact on the adsorption performance of TiS_2 in heterostructures.

The application of MN_4@G is often constrained by the low loading density of metal atoms and heterogeneous distribution of doping sites. In the region without dopants, the local structure of MN_4@G retains the carbon lattice of pure graphene. Therefore, we set up a model of G/TiS_2 in order to further examine the regulatory role of TiS_2 on the performance of such carbon atoms far away from the metal centers. As shown in Fig. 6b and Table S4, G/TiS_2 possesses enhanced trapping capabilities for LiPs with respect to G. Moreover, the adsorption energies of Li_2S_4, Li_2S_6 and Li_2S_8 on G/TiS_2 are −1.03, −0.94 and −1.01 eV, respectively, which are lower than those for organic electrolyte (−1.00 to −0.80 eV). Therefore, combining with TiS_2 can enhance the adsorption performance of the entire region of MN_4@G monolayers for LiPs, which will help overcome the disadvantages of low loading of atomically dispersed atoms in MN_4@G.

We have also investigated the SRR performance of those heterostructures by calculating the Gibbs free energy changes (ΔG) profile as depicted in Fig. 7. For MoN_4@G/TiS_2 and WN_4@G/TiS_2 (see Fig. 7a), the ΔG values of overall SRR are −1.06 and −1.19 eV, respectively, which are lower than those of −0.41 and −0.33 eV for MoN_4@G and WN_4@G, respectively. Moreover, the ΔG of rate-determining step (ΔG_{RDS}) for the transition from Li_2S_2 to Li_2S are 3.99 and 4.89 eV, lower than the corresponding values of 4.25 and 4.36 eV for individual MoN_4@G and WN_4@G, respectively. These results imply the positive effect of heterointerface on enhancing the SRR performance of MN_4@G (M = Mo and W). In contrast, the overall ΔG of SRR on VN_4@G/TiS_2 is 0.37 eV, which is larger than −0.82 eV for VN_4@G. Such an increase of ΔG can be attributed to the structural feature of VN_4@G/TiS_2 with the V atom located between VN_4@G and TiS_2 and formation of the V–S bond. It means that the single V atom in VN_4@G/TiS_2 will not participate in forming chemical bonds with LiPs and S_8 during the SRR process leading to decreased SRR performance compared to individual VN_4@G. When it turns to TiS_2/MN_4@G (M = Mo, W and V), the overall ΔG of SRR are −1.61, −1.66, and −1.17 eV, respectively, while the related ΔG_{RDS} values are 3.82, 3.75 and 4.32 eV. These values are comparable to the corresponding values for individual TiS_2. This shows that the heterointerface

effect on the SRR performance of TiS_2 is relatively weak. Regarding G and G/TiS_2, they exhibit even worse performance for SRR, as reflected by the ΔG values of 0.69 and 0.48 eV for the overall SRR, respectively (see Fig. 7b). This also implies that the SRR performance of carbon atoms far away from the metal centers in MN_4@G/TiS_2 (M = Mo, W and V) is relatively worse, which is still better than that for pristine graphene. Nevertheless, based on the above analysis, we believe that both sides of MN_4@G/TiS_2 possess promising performance for SRR. Overall, MN_4@G/TiS_2 (M = Mo and W) show good performance in stabilizing LiPs and accelerating the kinetics of SER/SRR as confirmed by the low values of adsorption energies for LiPs/S_8, ΔG for overall SRR, ΔG_{RDS} and E_b for Li_2S decomposition, which demonstrate that they are promising candidates electrocatalysts for sulfur chemistry in Li–S batteries.

4. Conclusions

Using DFT calculations, we explored the heterointerface effect on the catalytic performance SACs toward sulfur conversion in Li–S batteries. To this end, 15 heterostructures were constructed by combining MN_4@G (M = Mo, W and V) with 5 different 2D materials of TiS_2, C_3N_4, BN, graphene and rGO. We then investigated their electronic properties, adsorption capabilities for LiPs/S_8 and catalytic activities for sulfur redox. Using previously proposed descriptors of ΔE, we firstly screened three heterointerfaces MN_4@G/TiS_2 (M = Mo, W and V) due to their low values of E_b of 0.54, 0.44, and 0.41 eV, respectively, indicating the enhanced SER performance of MN4@G caused by the interface effect. This effect also induces the increased binding strength to LiPs/S_8 beneficial for suppressing the shuttle effect as reflected by the low adsorption energies. Moreover, our DFT calculations demonstrate that both sides of MN_4@G/TiS_2 (M = Mo and W) possess enhanced SRR performance compared to the individual components of heterostructures. These can be confirmed by those competitive values of low values of adsorption energies for soluble LiPs ($< \sim -3$ eV), ΔG for the overall SRR (-1.66 to 0.37) and ΔG_{RDS} (3.82 to 4.89). Interestingly, the interface effect even strengthens the binding strength of the carbon atoms far away from the metal centers and soluble LiPs, which will probably address the issue of low loading rate of atomically dispersed metal atoms. This study paves a new way of designing novel electrocatalyst for sulfur chemistry for Li–S batteries and even other alkali-ion-chalcogen batteries.

Author contributions

H. Liang and Z. Zeng performed the calculations and the data analysis and H. Liang prepared the draft of the manuscript. Z. Qiao and Y. Li initialize the project and proposed the supervision. All authors have given approval to the final version of the manuscript.

Conflicts of interest

The authors declare no competing financial interest.

Acknowledgements

This work was financially supported by the National Natural Science Foundation of China (Grants No. 52372254 and 91963210) and the Key Research and Development Program of Guangdong Province (No. 2020B0101690001). The calculations were carried out using supercomputers 'Tianhe-2' at NSCC Guangzhou.

References

1 X. Hong, R. Wang, Y. Liu, J. Fu, J. Liang and S. Dou, Recent advances in chemical adsorption and catalytic conversion materials for Li–S batteries, *J. Energy Chem.*, 2020, **42**, 144–168.
2 Y. Song, W. Cai, L. Kong, J. Cai, Q. Zhang and J. Sun, Rationalizing Electrocatalysis of Li–S Chemistry by Mediator Design: Progress and Prospects, *Adv. Energy Mater.*, 2020, **10**(11), 1901075.
3 L. Zhou, D. L. Danilov, R.-A. Eichel and P. H. L. Notten, Host Materials Anchoring Polysulfides in Li–S Batteries Reviewed, *Adv. Energy Mater.*, 2021, **11**(15), 2001304.
4 Z. W. Seh, Y. Sun, Q. Zhang and Y. Cui, Designing high-energy lithium–sulfur batteries, *Chem. Soc. Rev.*, 2016, **45**(20), 5605–5634.
5 Q. Pang, X. Liang, C. Y. Kwok and L. F. Nazar, Advances in lithium–sulfur batteries based on multifunctional cathodes and electrolytes, *Nat. Energy*, 2016, **1**(9), 16132.
6 Q. Shao, Z.-S. Wu and J. Chen, Two-dimensional materials for advanced Li–S batteries, *Energy Storage Mater.*, 2019, **22**, 284–310.
7 J. Xu, W. Zhang, H. Fan, F. Cheng, D. Su and G. Wang, Promoting lithium polysulfide/sulfide redox kinetics by the catalyzing of zinc sulfide for high performance lithium-sulfur battery, *Nano Energy*, 2018, **51**, 73–82.
8 H.-J. Peng, J.-Q. Huang and Q. Zhang, A review of flexible lithium–sulfur and analogous alkali metal–chalcogen rechargeable batteries, *Chem. Soc. Rev.*, 2017, **46**(17), 5237–5288.
9 Y. Huang, L. Lin, C. Zhang, L. Liu, Y. Li, Z. Qiao, J. Lin, Q. Wei, L. Wang, Q. Xie and D.-L. Peng, Recent Advances and Strategies toward Polysulfides Shuttle Inhibition for High-Performance Li–S Batteries, *Adv. Sci.*, 2022, 2106004.
10 Z. Liang, D. Yang, P. Tang, C. Zhang, J. Jacas Biendicho, Y. Zhang, J. Llorca, X. Wang, J. Li, M. Heggen, J. David, R. E. Dunin-Borkowski, Y. Zhou, J. R. Morante, A. Cabot and J. Arbiol, Atomically dispersed Fe in a C2N Based Catalyst as a Sulfur Host for Efficient Lithium–Sulfur Batteries, *Adv. Energy Mater.*, 2021, **11**(5), 2003507.
11 W. Ren, W. Ma, S. Zhang and B. Tang, Recent advances in shuttle effect inhibition for lithium sulfur batteries, *Energy Storage Mater.*, 2019, **23**, 707–732.

12 L. Zhang, D. Liu, Z. Muhammad, F. Wan, W. Xie, Y. Wang, L. Song, Z. Niu and J. Chen, Single Nickel Atoms on Nitrogen-Doped Graphene Enabling Enhanced Kinetics of Lithium–Sulfur Batteries, *Adv. Mater.*, 2019, **31**(40), 1903955.
13 Z. Du, X. Chen, W. Hu, C. Chuang, S. Xie, A. Hu, W. Yan, X. Kong, X. Wu, H. Ji and L.-J. Wan, Cobalt in Nitrogen-Doped Graphene as Single-Atom Catalyst for High-Sulfur Content Lithium–Sulfur Batteries, *J. Am. Chem. Soc.*, 2019, **141**(9), 3977–3985.
14 Z. Zeng, W. Nong, Y. Li and C. Wang, Universal-Descriptors-Guided Design of Single Atom Catalysts toward Oxidation of Li2S in Lithium–Sulfur Batteries, *Adv. Sci.*, 2021, **8**(23), 2102809.
15 S. Wu, C. Wang, H. Liang, W. Nong, Z. Zeng, Y. Li and C. Wang, High-Throughput Calculations for Screening d- and p-Block Single-Atom Catalysts toward Li2S/Na2S Decomposition Guided by Facile Descriptor beyond Brønsted–Evans–Polanyi Relationship, *Small*, 2023, 2305161.
16 J. Mei, T. Liao and Z. Sun, 2D/2D Heterostructures: Rational Design for Advanced Batteries and Electrocatalysis, *Energy Environ. Mater.*, 2022, **5**(1), 115–132.
17 Y. Li, J. Zhang, Q. Chen, X. Xia and M. Chen, Emerging of Heterostructure Materials in Energy Storage: A Review, *Adv. Mater.*, 2021, **33**(27), 2100855.
18 S. Huang, Z. Wang, Y. Von Lim, Y. Wang, Y. Li, D. Zhang and H. Y. Yang, Recent Advances in Heterostructure Engineering for Lithium–Sulfur Batteries, *Adv. Energy Mater.*, 2021, **11**(10), 2003689.
19 Y. Song, H. Zhou, X. Long, J. Xiao, J. Yang, N. Wu, Z. Chen, P. Li, C. Chen, J. Liao and M. Wu, Dual-heterostructures decorated interweaved carbon nanofibers sulfur host for high performance lithium-sulfur batteries, *Chem. Eng. J.*, 2021, **418**, 129388.
20 Y. Xue, D. Luo, N. Yang, G. Ma, Z. Zhang, J. Hou, J. Wang, C. Ma, X. Wang, M. Jin, Z. Chen and L. Shui, Engineering checkerboard-like heterostructured sulfur electrocatalyst towards high-performance lithium sulfur batteries, *Chem. Eng. J.*, 2022, **440**, 135990.
21 W. Yang, Y. Wei, Q. Chen, S. Qin, J. Zuo, S. Tan, P. Zhai, S. Cui, H. Wang, C. Jin, J. Xiao, W. Liu, J. Shang and Y. Gong, A MoO3/MoO2-CP self-supporting heterostructure for modification of lithium–sulfur batteries, *J. Mater. Chem. A*, 2020, **8**(31), 15816–15821.
22 J. Qin, R. Wang, P. Xiao and D. Wang, Engineering Cooperative Catalysis in Li–S Batteries, *Adv. Energy Mater.*, 2023, 2300611.
23 H. X. Dang, A. J. Sellathurai and D. P. J. Barz, An ion exchange membrane-free, ultrastable zinc-iodine battery enabled by functionalized graphene electrodes, *Energy Storage Mater.*, 2023, **55**, 680–690.
24 X. Xia, J. Yang, Y. Liu, J. Zhang, J. Shang, B. Liu, S. Li and W. Li, Material Choice and Structure Design of Flexible Battery Electrode, *Adv. Sci.*, 2023, **10**(3), 2204875.
25 Y. V. Lim, X. L. Li and H. Y. Yang, Recent Tactics and Advances in the Application of Metal Sulfides as High-Performance Anode Materials for Rechargeable Sodium-Ion Batteries, *Adv. Funct. Mater.*, 2021, **31**(10), 2006761.
26 M. Yang, X. Chang, L. Wang, X. Wang, M. Gu, H. Huang, L. Tang, Y. Zhong and H. Xia, Interface Modulation of Metal Sulfide Anodes for Long-Cycle-Life Sodium-Ion Batteries, *Adv. Mater.*, 2023, **35**(13), 2208705.
27 B. Li, Y. Wang, N. Jiang, L. An, J. Song, Y. Zuo, F. Ning, H. Shang and D. Xia, Electrolytic-anion-redox adsorption pseudocapacitance in nanosized lithium-free transition metal oxides as cathode materials for Li-ion batteries, *Nano Energy*, 2020, **72**, 104727.
28 Y. Pei, Q. Chen, M. Wang, P. Zhang, Q. Ren, J. Qin, P. Xiao, L. Song, Y. Chen, W. Yin, X. Tong, L. Zhen, P. Wang and C.-Y. Xu, A medium-entropy transition metal oxide cathode for high-capacity lithium metal batteries, *Nat. Commun.*, 2022, **13**(1), 6158.
29 Y. Wang, T. Guo, E. Alhajji, Z. Tian, Z. Shi, Y.-Z. Zhang and H. N. Alshareef, MXenes for Sulfur-Based Batteries, *Adv. Energy Mater.*, 2023, **13**(4), 2202860.
30 F. Ming, H. Liang, G. Huang, Z. Bayhan and H. N. Alshareef, MXenes for Rechargeable Batteries Beyond the Lithium-Ion, *Adv. Mater.*, 2021, **33**(1), 2004039.
31 M. Telkhozhayeva, B. Hirsch, R. Konar, E. Teblum, R. Lavi, M. Weitman, B. Malik, E. Moretti and G. D. Nessim, 2D TiS_2 flakes for tetracycline hydrochloride photodegradation under solar light, *Appl. Catal., B*, 2022, **318**, 121872.
32 J. Wang and S. Wang, A critical review on graphitic carbon nitride (g-C3N4)-based materials: Preparation, modification and environmental application, *Coord. Chem. Rev.*, 2022, **453**, 214338.
33 L. Liu, J. Park, D. A. Siegel, K. F. McCarty, K. W. Clark, W. Deng, L. Basile, J. C. Idrobo, A.-P. Li and G. Gu, Heteroepitaxial Growth of Two-Dimensional Hexagonal Boron Nitride Templated by Graphene Edges, *Science*, 2014, **343**(6167), 163–167.
34 Y. Zheng, H. Li, H. Yuan, H. Fan, W. Li and J. Zhang, Understanding the anchoring effect of Graphene, BN, C2N and C3N4 monolayers for lithium−polysulfides in Li−S batteries, *Appl. Surf. Sci.*, 2018, **434**, 596–603.
35 R. Jain, P. Hundekar, T. Deng, X. Fan, Y. Singh, A. Yoshimura, V. Sarbada, T. Gupta, A. S. Lakhnot, S. O. Kim, C. Wang and N. Koratkar, Reversible Alloying of Phosphorene with Potassium and Its Stabilization Using Reduced Graphene Oxide Buffer Layers, *ACS Nano*, 2019, **13**(12), 14094–14106.
36 J. Hafner, Ab-initio simulations of materials using VASP: Density-functional theory and beyond, *J. Comput. Chem.*, 2008, **29**(13), 2044–2078.
37 G. Kresse and J. Furthmüller, Efficient iterative schemes for ab initio total-energy calculations using a plane-wave basis set, *Phys. Rev. B: Condens. Matter Mater. Phys.*, 1996, **54**(16), 11169–11186.
38 J. P. Perdew, J. A. Chevary, S. H. Vosko, K. A. Jackson, M. R. Pederson, D. J. Singh and C. Fiolhais, Atoms, molecules, solids, and surfaces: Applications of the generalized gradient approximation for exchange and correlation, *Phys. Rev. B: Condens. Matter Mater. Phys.*, 1992, **46**(11), 6671–6687.
39 J. P. Perdew and Y. Wang, Accurate and simple analytic representation of the electron-gas correlation energy,

Phys. Rev. B: Condens. Matter Mater. Phys., 1992, **45**(23), 13244–13249.

40 J. P. Perdew, K. Burke and M. Ernzerhof, Generalized Gradient Approximation Made Simple, *Phys. Rev. Lett.*, 1996, **77**(18), 3865–3868.

41 P. E. Blöchl, Projector augmented-wave method, *Phys. Rev. B: Condens. Matter Mater. Phys.*, 1994, **50**(24), 17953–17979.

42 G. Kresse and D. Joubert, From ultrasoft pseudopotentials to the projector augmented-wave method, *Phys. Rev. B: Condens. Matter Mater. Phys.*, 1999, **59**(3), 1758–1775.

43 S. Grimme, Semiempirical GGA-type density functional constructed with a long-range dispersion correction, *J. Comput. Chem.*, 2006, **27**(15), 1787–1799.

44 G. Henkelman and H. Jónsson, Improved tangent estimate in the nudged elastic band method for finding minimum energy paths and saddle points, *J. Chem. Phys.*, 2000, **113**(22), 9978–9985.

45 G. Henkelman, B. P. Uberuaga and H. Jónsson, A climbing image nudged elastic band method for finding saddle points and minimum energy paths, *J. Chem. Phys.*, 2000, **113**(22), 9901–9904.

46 III, R. D. J., NIST Computational Chemistry Comparison and Benchmark Database. **https://cccbdb.nist.gov**.

47 Q. He, B. Yu, H. Wang, M. Rana, X. Liao and Y. Zhao, Oxygen defects boost polysulfides immobilization and catalytic conversion: First-principles computational characterization and experimental design, *Nano Res.*, 2020, **13**(8), 2299–2307.

48 T. Björkman, A. Gulans, A. V. Krasheninnikov and R. M. Nieminen, van der Waals Bonding in Layered Compounds from Advanced Density-Functional First-Principles Calculations, *Phys. Rev. Lett.*, 2012, **108**(23), 235502.

49 Y. Qie, J. Liu, S. Wang, S. Gong and Q. Sun, C3B monolayer as an anchoring material for lithium-sulfur batteries, *Carbon*, 2018, **129**, 38–44.